Spectroscopic evidence for Fermi liquid-like energy and temperature dependence of the relaxation rate in the pseudogap phase of the cuprates

Seyed Iman Mirzaei[a], Damien Stricker[a], Jason N. Hancock[a,b], Christophe Berthod[a], Antoine Georges[a,c,d], Erik van Heumen[a,e], Mun K. Chan[f], Xudong Zhao[f,g], Yuan Li[h], Martin Greven[f], Neven Barišić[f,i,j], and Dirk van der Marel[a,1]

[a]Département de Physique de la Matière Condensée, Université de Genève, 1211 Geneva, Switzerland; [b]Department of Physics and the Institute of Materials Science, Storrs, CT 06119; [c]Centre de Physique Théorique, École Polytechnique, Centre National de la Recherche Scientifique, 91128 Palaiseau, France; [d]Collège de France, 75005 Paris, France; [e]Van der Waals-Zeeman Instituut, Universiteit van Amsterdam,1098 XH Amsterdam, The Netherlands; [f]School of Physics and Astronomy, University of Minnesota, Minneapolis, MN 55455; [g]State Key Lab of Inorganic Synthesis and Preparative Chemistry, College of Chemistry, Jilin University, Changchun 130012, China; [h]International Center for Quantum Materials, School of Physics, Peking University, Beijing 100871, China; [i]Institute of Physics, 10000 Zagreb, Croatia; and [j]Service de Physique de l'Etat Condensé, Commissariat à l'Energie Atomique, Direction des Sciences de la Matière (DSM)-Institut Rayonnement Matière de Saclay (IRAMIS), 91198 Gif-sur-Yvette, France

Edited by David Pines, University of California, Davis, CA, and approved February 25, 2013 (received for review October 29, 2012)

Cuprate high-T_c superconductors exhibit enigmatic behavior in the nonsuperconducting state. For carrier concentrations near "optimal doping" (with respect to the highest T_cs) the transport and spectroscopic properties are unlike those of a Landau–Fermi liquid. On the Mott-insulating side of the optimal carrier concentration, which corresponds to underdoping, a pseudogap removes quasiparticle spectral weight from parts of the Fermi surface and causes a breakup of the Fermi surface into disconnected nodal and antinodal sectors. Here, we show that the near-nodal excitations of underdoped cuprates obey Fermi liquid behavior. The lifetime $\tau(\omega, T)$ of a quasi-particle depends on its energy ω as well as on the temperature T. For a Fermi liquid, $1/\tau(\omega, T)$ is expected to collapse on a universal function proportional to $(\hbar\omega)^2 + (p\pi k_B T)^2$. Magneto-transport experiments, which probe the properties in the limit $\omega = 0$, have provided indications for the presence of a T^2 dependence of the dc ($\omega = 0$) resistivity of different cuprate materials. However, Fermi liquid behavior is very much about the energy dependence of the lifetime, and this can only be addressed by spectroscopic techniques. Our optical experiments confirm the aforementioned universal ω- and T dependence of $1/\tau(\omega, T)$, with $p \sim 1.5$. Our data thus provide a piece of evidence in favor of a Fermi liquid-like scenario of the pseudogap phase of the cuprates.

optical spectroscopy | superconductivity | mass renormalization | self energy

The compound $HgBa_2CuO_{4+\delta}$ (Hg1201) is the single-layer cuprate that exhibits the highest T_c (97 K). We therefore measured the optical conductivity of strongly underdoped single crystals of Hg1201 ($T_c = 67$ K). Here we are interested in the optical conductivity of the CuO_2 layers. We therefore express the optical conductivity as a 2D sheet conductance $G(\omega) = d_c\sigma(\omega)$, where d_c is the interlayer spacing. The real part of the sheet conductance normalized by the conduction quantum $G_0 = 2e^2/h$ is shown in Fig. 1. As seen in the figure, a gap-like suppression below 140 meV is clearly observable for temperatures below T_c and remains visible in the normal state up to ~250 K. This is a clear optical signature of the pseudogap. We also observe the zero-energy mode due to the free charge carrier response, which progressively narrows upon lowering the temperature. In materials where the charge carrier relaxation is dominated by impurity scattering, the width of this "Drude" peak corresponds to the relaxation rate of the charge carriers. Relaxation processes arising from interactions have the effect of replacing the constant (frequency-independent) relaxation rate with a frequency-dependent one. The general expression for the optical conductivity of interacting electrons is then

$$G(\omega, T) = \frac{i\pi K}{\hbar\omega + M(\omega, T)} G_0. \quad [1]$$

The spectral weight K corresponds to minus the kinetic energy if the frequency integration of the experimental data is restricted to intraband transitions. The effect of electron–electron interactions and coupling to collective modes is described by the memory function $M(\omega, T) = M_1(\omega, T) + iM_2(\omega, T)$, where $\hbar^{-1}M_2(\omega, T) = 1/\tau(\omega, T)$ represents the dynamical (or optical) relaxation rate in the case of a Fermi liquid.

The zero frequency limit of the optical conductivity of Fig. 1 corroborates the recently reported temperature dependence of the dc resistivity (1) as shown in Fig. 2. Because K is practically temperature independent in the normal state (2), the low-temperature T^2 dependence of the resistivity is due to the quadratic temperature variation of $M_2(0, T) = \hbar/\tau(0, T)$. The infrared data confirm that Hg1201 exhibits the lowest residual resistance among the cuprates and a change to a linear temperature dependence above T^* associated with the sudden closing of a pseudogap (3, 4). Fig. 2*B* shows this as a clear departure from the T^2 curve at $\sim 5 \times 10^4$ K^2. The dc transport data, owing to the higher precision, allow for Hg1201 crystals of the same composition and doping to identify $T^* \sim 350$ K as the temperature above which the resistivity has a linear temperature dependence, and $T^{**} \sim 220$ K as the temperature below which the temperature dependence is purely quadratic. Finally, superconducting fluctuations become noticeable at $T' \sim 85$ K.

The doping dependences of K and of the coherent spectral weight, defined as $K^* = K/(1 + M_1(\omega, T)\hbar\omega)|_{\omega=0}$, are summarized in Fig. 3 for a number of hole-doped cuprates. The theoretical values of K based on the band parameters obtained from local density approximation (LDA) ab initio calculations are about a factor of 2 larger than the measured values, which is due to strong correlation predicted by the Hubbard model for $U/t \geq 4$ (6). K decreases when the hole doping decreases, but does not extrapolate to zero for zero doping in accordance with the

Author contributions: S.I.M., D.S., N.B., and D.v.d.M. designed research; S.I.M., D.S., J.N.H., C.B., A.G., E.v.H., M.K.C., X.Z., Y.L., M.G., N.B., and D.v.d.M. performed research; S.I.M., D.S., J.N.H., C.B., A.G., E.v.H., M.K.C., X.Z., Y.L., M.G., N.B., and D.v.d.M. analyzed data; and S.I.M., D.S., C.B., A.G., M.G., N.B., and D.v.d.M. wrote the paper.

The authors declare no conflict of interest.

This article is a PNAS Direct Submission.

Freely available online through the PNAS open access option.

[1]To whom correspondence should be addressed. E-mail: Dirk.VanDerMarel@unige.ch.

This article contains supporting information online at www.pnas.org/lookup/suppl/doi:10.1073/pnas.1218846110/-/DCSupplemental.

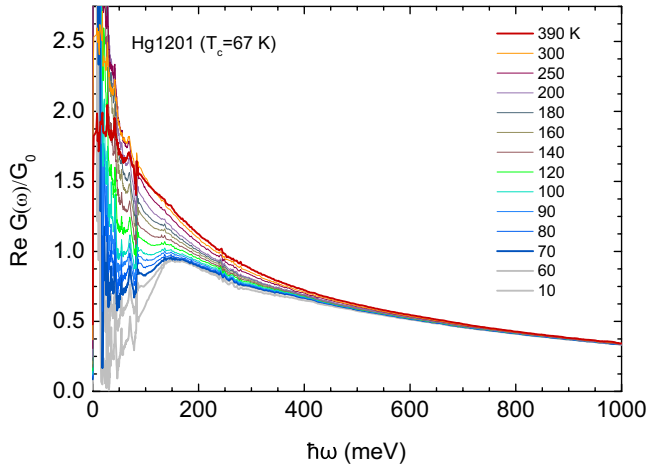

Fig. 1. Optical sheet conductance of underdoped Hg1201 (T_c = 67 K). Temperatures from 10 to 390 K. Data below T_c are shown in gray.

analysis of Comanac et al. (7). In contrast, the coherent spectral weight K^* is proportional to the hole doping x: $K = xK^0$, where $K^0 = 496$ meV, in agreement with the trend observed for $La_{2-x}Sr_2CuO_4$ (8) and $YBa_2Cu_3O_{7-\delta}$ (9). This provides strong evidence that a Mott insulator is approached as the doping is reduced. It cannot be determined from these data whether this occurs because (*i*) the quasi-particle residue is gradually suppressed (10, 11) or (*ii*) the Fermi surface arcs shrink to zero without vanishing of the nodal spectral weight (12, 13).

The real and imaginary parts of the memory function of underdoped Hg1201 with $T_c = 67$ K are shown in Fig. 4 for temperatures from 10 to 390 K. $M_1(\omega, T)$ has a linear slope extrapolating to $\omega = 0$, which becomes less steep at higher temperatures. The maximum at ~105 meV erodes gradually as temperature increases, but a residue of this structure remains visible even at 390 K. In Fig. 4*E* we show a plot of the frequency- and temperature-dependent mass enhancement factor $m^*(\omega, T) = M_1(\omega, T)/\hbar\omega + 1$. Above 60 meV

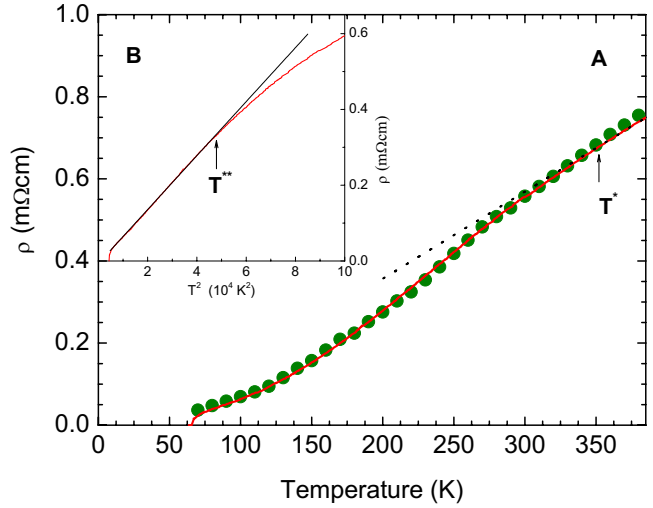

Fig. 2. dc resistivity of underdoped Hg1201 (T_c = 67 K). Inverse optical conductivity extrapolated to zero frequency (green circles) compared with measured dc resistivity (1) (solid red line) of a sample of the same composition and doping (*A*). The dashed black curve is a *T*-linear fit to the resistivity data above 350 K. (*B*) Same dc resistivity data as a function of T^2, shown with a T^2 fit to the data below 220 K. Definitions and values for *T** and *T*** of ref. 1 are used.

$m^*(\omega, T)$ is a monotonously decreasing function of temperature. For ω that is not too large, $m^*(T)$ is, roughly speaking, a plateau at low temperature, with a weak maximum at T(max) followed by a linear-like decrease at higher temperature. T(max) increases when ω decreases and for $\omega \to 0$ extrapolates to 212 K $\sim T^{**}$, indicating another way of identifying T^{**}. The increase of $m^*(\omega, T)$ from about 3 at 390 K to 5 at T^{**}, taken together with the strong temperature dependence of $M_1(\omega, T)$ near its maximum at 105 meV, indicates that the charge carriers become increasingly renormalized when the temperature decreases. Our results also corroborate the observation in ref. 14 that the integrated optical conductivity does not decrease when T decreases, so that no opening of an optical pseudogap is seen when, at T^*, part of the Fermi surface is removed by a pseudogap, despite the emergence at this temperature of a novel ordered state with two Ising-like magnetic collective modes at 54 and 39 meV as observed with inelastic neutron scattering (15).

Turning now to the dynamical relaxation rate $\hbar^{-1}M_2(\omega, T) = 1/\tau(\omega, T)$, we observe from Fig. 4 that its frequency dependence exhibits an upward curvature for all temperatures. Also, the temperature dependence has a T^2 component at the lowest frequencies. Earlier indications for T^2 dependence of the scattering rate came from the dc ($\omega = 0$) resistivity (1, 16, 17). For frequencies above 50 meV this component is either absent or completely masked by the onset of superconductivity (gray segments of the temperature traces). Although $M_2(\omega, T)$ has no maximum as a function of temperature, the curves have an inflection point which shifts from roughly 200 to 100 K when the frequency is raised from 10 to 50 meV. The saturation of $m^*(\omega, T)$ and the merger of the resistivity with a T^2 dependence indicate that the system enters a Fermi liquid-like state at ~200 K. We notice that at temperatures above T_c the initial rise is given by a linear slope as a function of ω^2 (Fig. 5, *Inset*). For an ideal Fermi liquid, $M(\omega, T)$ in the relevant range of ω and T is, to a good approximation,

$$M(\omega, T) \cong \left(\frac{1}{\tilde{Z}} - 1\right)\hbar\omega + iC\left[(\hbar\omega)^2 + (p\pi k_B T)^2\right], \qquad [2]$$

where $\tilde{Z}$ is proportional to the quasi-particle residue, C is a constant with units of inverse energy, and $p = 2$ (ref. 18 and *Supporting Information*). To check possible Fermi liquid characteristics of the data, we introduce a single parameter ξ defined as $\xi^2 = (\hbar\omega)^2 + (p\pi k_B T)^2$, and we investigate M_2 as a function of ξ. As shown in Fig. 6 for three underdoped cuprate materials [Hg1201, *ortho*-II Y $Ba_2Cu_3O_{6.5}$ (Y123) (ref. 19), and Bi2201 (ref. 20)] with hole concentration $x \approx 0.1$, the M_2 data of the normal state collapse in the low-energy range on a single scaling curve for $p = 1.5$. This value of p was obtained by searching for the best scaling collapse for $1 \le p \le 2$ in steps of 0.1 (*Supporting Information*). Comparing the functional form of $M_2(\xi)$ for these three materials, we make the following observations: (*i*) Going from Hg1201 to Bi2201 (Fig. 6, *Left* and *Right*, respectively) in this plot, the residual ($\xi = 0$) value of $M_2(\xi)$ increases from 0 to about 80 meV. Indeed, it is generally thought that the relatively low values of T_c in single-layer Bi2201 have to do with strong scattering by disorder (1, 21). (*ii*) We also notice that in the case of Bi2201 some negative curvature appears at the lowest energies, which is an indication that the Fermi liquid characteristics are affected to some extent, and appear to be relatively fragile with respect to disorder. (*iii*) The implications of the loss of scaling above 100 meV in the Bi2201 data are not entirely clear. In principle there is no reason to expect scaling, because this is clearly beyond the range of "universal" Fermi liquid behavior. However, the single-parameter scaling seems to persist into this regime for the other two materials (Y123 and Hg1201), leading to the speculation that impurity scattering also contributes to the disappearance of scaling above 100 meV for the Bi2201 sample.

PHYSICS

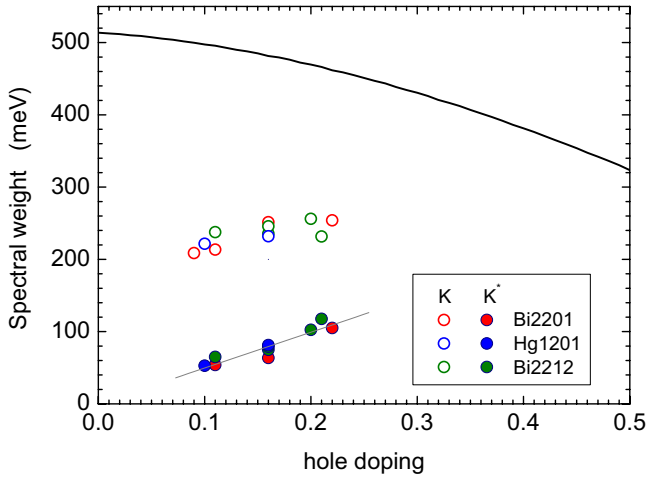

Fig. 3. Conduction band spectral weight per CuO_2 layer for a large number of cuprate superconductors. Closed symbols: coherent spectral weight K^*. The gray line is a linear least-squares fit, $K^* = 496x$, where x is the nominal hole doping. Open symbols: total spectral weight, K. Data are presented for Hg1201 with 10% doping (see *Supporting Information*). For the other materials see table 1 in ref. 5. The black solid curve represents K calculated from ab initio band parameters for Hg1201 (*Supporting Information*). For the $Bi_2Sr_2CuO_{6+\delta}$ (Bi2201) sample with hole doping below 0.10, K^* could not be calculated, because in this case we obtain $M_1(\omega, T) < 0$ for $\omega \to 0$, possibly due to disorder.

The most important observation borne out by these data is that the frequency dependence of $M_1(\omega, T)$ and $M_2(\omega, T)$ follows by and large the behavior expected for a Fermi liquid: At low frequencies and temperatures $M_1(\omega, T)$ is indeed a linear function of ω, and $M_2(\omega, T)$ scales with $(\hbar\omega)^2 + (p\pi k_B T)^2$. Other hints at possible Fermi liquid behavior came from the recent discovery of quantum oscillations at low temperature and high magnetic field in underdoped $YBa_2Cu_3O_{6+\delta}$ (13) and $YBa_2Cu_4O_8$ (22), from the observation of the Fermi–Dirac statistics underlying the quantum oscillations (23), and from the two-fluid analysis (24) of NMR data (25). We note that recent theories (e.g., refs. 26–28) have emphasized the possible relevance of Fermi liquid concepts—or a hidden form of these in the superconducting regime (29)—to the metallic state of hole-doped cuprates. Our experimental observations provide a strong incentive for further theoretical work in this direction. We highlight two striking aspects of the data: (*i*) The slope $\partial M_1(\omega, T)/\partial\omega$ for $\omega \to 0$ decreases significantly as a function of increasing temperature; and (*ii*) $p < 2$. We speculate that these issues are related to the progressive filling-in of the pseudogap as a function of increasing temperature. Already in a two-fluid picture of a nodal Fermi liquid in parallel to an antinodal liquid, nonuniversal features (for Fermi liquids) are introduced in the optical conductivity, because the properties at the Fermi surface change gradually from Fermi liquid at the nodes (30) to strongly incoherent and pseudogapped at the hot spots near the antinodes (31). In fact, also in other compounds p is found to be different from 2 (32–34). Recently, Maslov and Chubukov interpreted this as a combination of Fermi liquid scattering and an additional source of elastic scattering from magnetic moments or resonant levels (35).

Theoretically, it is expected that the T^2- and ω^2 dependence of $M_2(\omega, T)$ is limited to $\hbar\omega$ and $p\pi k_B T$ lower than some energy scale ξ_0, which in the context of single-parameter scaling behavior of a Fermi liquid is proportional to the effective Fermi energy. Electronic correlations strongly reduce this energy scale compared with the bare Fermi energy. For most materials the issue of the Fermi liquid-like frequency dependence of $M_2(\omega, T)$ has remained largely unexplored. This is related to the difficulty that in cases such as the heavy fermion materials where this type of coupling dominates, the range of Fermi liquid behavior is smaller than 10 meV, making it particularly difficult to obtain the required measurement accuracy in an infrared experiment. Clean underdoped cuprates present in this respect a favorable exception because, as can be seen from Figs. 5 and 6, the relevant energy scale ξ_0 is about 100 meV for a doping level around 10%. Above this energy, $M_2(\omega, T)$ crosses over to a more linear trend as a function of both ω and T. This suggests that in cuprates the range of applicability of Fermi liquid behavior is limited by a different scattering mechanism that develops at high T and high ω as the pseudogap gets filled.

The ξ^2-dependence of the relaxation rate can be understood as follows: An electron at a distance ξ above the Fermi energy can, as a result of electron–electron interactions, decay to a final state ξ–Ω by creating an electron–hole pair of energy Ω. The density of states of electron–hole pairs is the spin (charge) susceptibility

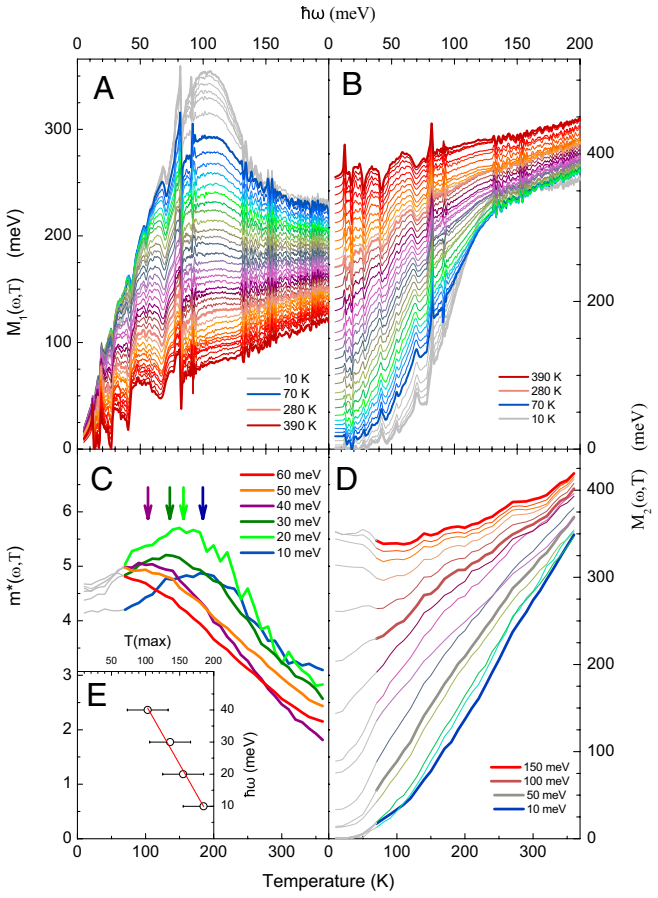

Fig. 4. Optical self-energy as a function of frequency and temperature. (*A*) Real and (*B*) imaginary part of the memory function as a function of $\hbar\omega$ for underdoped Hg1201 ($T_c = 67$ K). Spectra are shown in 10-K intervals for temperatures from 10 to 390 K. Thick lines are used to highlight the 10-, 70-, 280-, and 390-K data. (*C*) Effective mass $m^*(\omega, T)$ as a function of temperature for selected values of $\hbar\omega$ in 10-meV intervals from 10 to 60 meV. (*D*) Relaxation rate $M_2(\omega, T)$ as a function of temperature for selected values of $\hbar\omega$ in 10-meV intervals from 10 to 150 meV. Thick lines are used to highlight the data at selected energies. In *C* the approximate temperatures of the maxima T(max) are indicated with an arrow for ω with the corresponding color. (*E*) shows the same T(max) versus ω. The solid line is a linear fit, which extrapolates to $T(\max) = 212$ K for $\omega \to 0$. All data in the superconducting state are in gray. The temperature range (370 K) of *C* and *D* is chosen to match the frequency range of *A* and *B* (200 meV) according to the scaling relation $2\pi k_B T = \hbar\omega$.

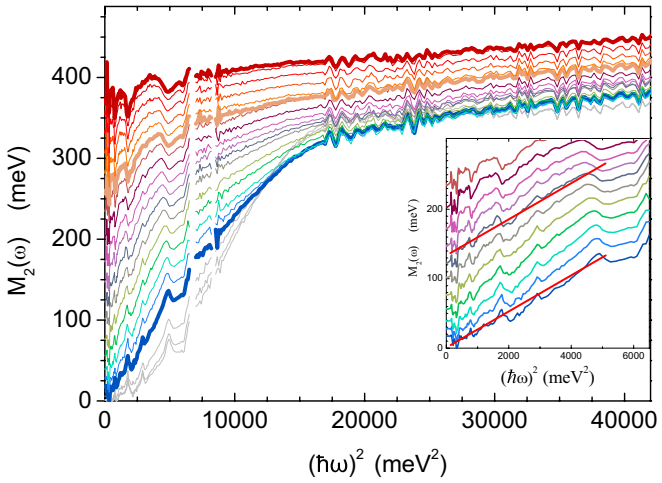

Fig. 5. Dynamical relaxation rate of underdoped Hg1201. Imaginary part of the memory function of underdoped Hg1021 ($T_c = 67$ K) for temperatures between 10 and 390 K in 20-K steps as a function of ω^2. Thick lines are used to highlight the 70-, 280-, and 390-K data. (*Inset*) Zoom of the low-ω range showing a linear fit; temperatures are from 70 to 270 K in 20-K steps.

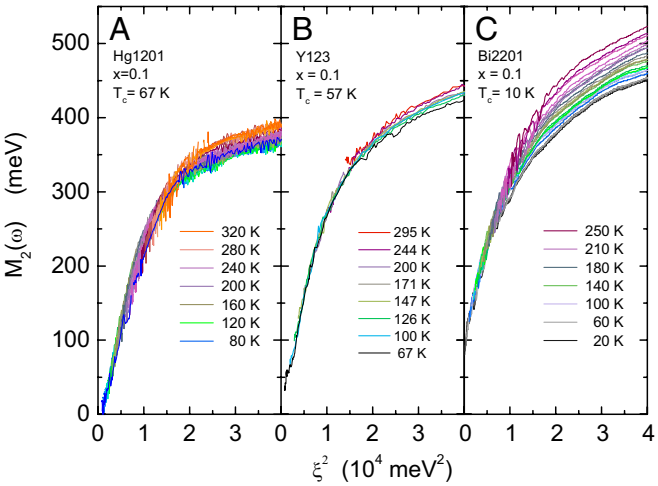

Fig. 6. Collapse of the frequency and temperature dependence of the relaxation rate of underdoped cuprate materials. Normal state $M_2(\omega, T)$ as a function of $\xi^2 \equiv (\hbar\omega)^2 + (p\pi k_B T)^2$ with $p = 1.5$. (*A*) Hg1201 ($x \cong 0.1, T_c = 67$ K). (*B*) Y123 ($x \cong 0.1, T_c = 57$ K), spectra by Hwang et al. (19) (digitized data of Fig. 6 represented here as a function of ξ^2). (*C*) Bi2201 ($x \cong 0.1, T_c = 10$ K); data of van Heumen et al. (20) represented here as a function of ξ^2. The data displayed in *A* and *C* are in 10-K intervals with color coding indicated for temperatures in 40-K steps. In between these steps the color evolves gradually as a function of temperature. In *B* the color coding is given for all temperatures displayed.

$\chi''(\Omega)$, where spin (charge) refers to electron–hole pairs carrying (no) net spin. $\chi''(\Omega)$ can be strongly renormalized, but the property that $\chi''(\Omega) \propto \Omega$ in the limit $\Omega \to 0$ is generic for Fermi liquids (24). Integration of the susceptibility multiplied with the interaction vertex $I^2\chi''(\Omega)$ over all possible decay channels from zero to ξ leads us to conclude that indeed $M_2 \propto \xi^2$, as reported experimentally in the present article. In this description the cross-over ξ_0 corresponds to the energy where $I^2\chi''(\Omega)$ is truncated, leading to a leveling off of M_2 for $\xi > \xi_0$. The strong temperature dependence of $M_1(\omega, T)$ is also a natural consequence of this description; it was shown in ref. 36 that, in leading orders of temperature, $\chi''(\Omega)$ of a correlated Fermi liquid decreases as a function of temperature.

In summary, we have shown from optical spectroscopy measurements that the ungapped near-nodal excitations of underdoped cuprate superconductors obey Fermi liquid behavior when materials with reduced amount of disorder are considered. This observation, which is at variance with some established paradigms, provides leads toward understanding of the metallic state and high-temperature superconductivity in these materials.

Materials and Methods

Sample Preparation. Single crystals were grown using a flux method, characterized, and heat treated to the desired doping level as described in refs. 37 and 38. The conductivity data in Fig. 1 are of a sample which has an onset critical temperature of 67 K and a transition width of 2 K. The crystal surface is oriented along the *a*–*b* plane with a dimension of about 1.51×1.22 mm^2. Hg1201 samples are hygroscopic. Therefore, the last stage of the preparation of the sample surface is done under a continuous flow of nitrogen, upon which the sample is transferred to a high-vacuum chamber (10^{-7} mbar) within a few minutes. Before each measurement the surface is carefully checked for any evidence of oxidation.

Comparison with dc Resistivity. Transport measurements have been performed using the four-terminal method. Due to the irregular shape of the cleaved samples the absolute value of the dc resistivity can only be determined with about 20% accuracy. However, we obtained very high relative accuracy of the temperature dependence of the dc resistivity, as seen from identical temperature dependences of samples of the same composition and doping, regardless of having significantly different dimensions and shapes. An independent check of the dc resistivity was obtained from the $\omega = 0$ limit of the experimental infrared optical conductivity (Fig. 2). The dc resistivity had to be scaled by a factor of 0.66 to match the optical data, most likely due to the aforementioned influence of the irregular shape of the crystals on the absolute value of the measured dc resistances. The excellent match of the two temperature dependences demonstrates the high quality of both dc resistivity and optical conductivity data.

ACKNOWLEDGMENTS. We thank A. Chubukov, A. J. Leggett, T. Giamarchi, T. M. Rice, and T. Timusk for discussions and communications. This work was supported by the Swiss National Science Foundation (SNSF) through Grant 200020-140761 and the National Center of Competence in Research, Materials with Novel Electronic Properties. The crystal growth and characterization work was supported by the US Department of Energy, Office of Basic Energy Sciences. X.Z. acknowledges support from the National Natural Science Foundation, China; N.B. acknowledges support from the European Commission under the [Intra-European Fellowships (IEF)] Marie Curie Fellowship Programme; and E.v.H. acknowledges support through the Vernieuwingsimpuls (VENI) program funded by the Netherlands Organisation for Scientific Research.

1. Barišić N, et al. (2012) Universal sheet resistance of the cuprate superconductors. arXiv:1207.1504.
2. Norman M, Chubukov A, van Heumen E, Kuzmenko AB, van der Marel D (2007) Optical integral in the cuprates and the question of sum-rule violation. *Phys Rev B* 76(22):220509.
3. Bucher B, Steiner P, Karpinski J, Kaldis E, Wachter P (1993) Influence of the spin gap on the normal state transport in $YBa_2Cu_4O_8$. *Phys Rev Lett* 70(13):2012–2015.
4. Ando Y, Komiya S, Segawa K, Ono S, Kurita Y (2004) Electronic phase diagram of high-T_c cuprate superconductors from a mapping of the in-plane resistivity curvature. *Phys Rev Lett* 93(26 Pt 1):267001.
5. van Heumen E, et al. (2009) Optical determination of the relation between the electron-boson coupling function and the critical temperature in high-T_c cuprates. *Phys Rev B* 79(18):184512.
6. Rozenberg MJ, et al. (1995) Optical conductivity in Mott-Hubbard systems. *Phys Rev Lett* 75(1):105–108.
7. Comanac A, de' Medici L, Capone M, Millis AJ (2008) Optical conductivity and the correlation strength of high-temperature copper-oxide superconductors. *Nat Phys* 4(4):287–290.
8. Uchida S, et al. (1991) Optical spectra of $La_{2-x}Sr_xCuO_4$: Effect of carrier doping on the electronic structure of the CuO_2 plane. *Phys Rev B Condens Matter* 43(10):7942–7954.
9. Padilla WJ, et al. (2005) Constant effective mass across the phase diagram of high-T_c cuprates. *Phys Rev B* 72(6):060511.
10. Brinkman WF, Rice TM (1970) Application of Gutzwiller's variational method to the metal-insulator transition. *Phys Rev B* 2(10):4302–4304.
11. Fournier D, et al. (2010) Loss of nodal quasiparticle integrity in underdoped $YBa_2Cu_3O_{6+x}$. *Nat Phys* 6(11):905–911.
12. Kanigel A, et al. (2006) Evolution of the pseudogap from Fermi arcs to the nodal liquid. *Nat Phys* 2(7):447–451.

13. Doiron-Leyraud N, et al. (2007) Quantum oscillations and the Fermi surface in an underdoped high-T_c superconductor. *Nature* 447(7144):565–568.
14. Santander-Syro AF, et al. (2001) Absence of a loss of in-plane infrared spectral weight in the pseudogap regime of $Bi_2Sr_2CaCu_2O_{8-\delta}$. *Phys Rev Lett* 88(9):097005.
15. Li Y, et al. (2012) Two Ising-like magnetic excitations in a single-layer cuprate superconductor. *Nat Phys* 8(5):404–410.
16. Ando Y, Kurita Y, Komiya S, Ono S, Segawa K (2004) Evolution of the Hall coefficient and the peculiar electronic structure of the cuprate superconductors. *Phys Rev Lett* 92(19):197001.
17. Hussey NE (2011) What drives pseudogap physics in high-T_c cuprates? A view from the (resistance)bridge. *J Phys Chem Solids* 72(5):529–532.
18. Berthod C, et al. (2013) Non-Drude universal scaling laws for the optical response of local Fermi liquids *Phys Rev B* 87(11):115109.
19. Hwang J, et al. (2006) A-axis optical conductivity of detwinned ortho-II $YBa_2Cu_3O_{6.50}$. *Phys Rev B* 73:014508.
20. van Heumen E, Meevasana W, Kuzmenko AB, Eisaki H, van der Marel D (2009) Doping-dependent optical properties of Bi2201. *New J Phys* 11(5):055067.
21. Eisaki H, et al. (2004) Effect of chemical inhomogeneity in bismuth-based copper oxide superconductors. *Phys Rev B* 69(8):064512.
22. Bangura AF, et al. (2008) Small Fermi surface pockets in underdoped high temperature superconductors: Observation of Shubnikov-de Haas oscillations in $YBa_2Cu_4O_8$. *Phys Rev Lett* 100(4):047004.
23. Sebastian SE, et al. (2010) Fermi-liquid behavior in an underdoped high-T_c superconductor. *Phys Rev B* 81(14):140505.
24. Barzykin V, Pines D (2009) Universal behaviour and the two-component character of magnetically underdoped cuprate superconductors. *Adv Phys* 58(1):1–65.
25. Haase J, et al. (2012) Two-component uniform spin susceptibility of superconducting $HgBa_2CuO_{2+\delta}$ single crystals measured using ^{63}Cu and ^{199}Hg nuclear magnetic resonance. *Phys Rev B* 85(10):104517.
26. Gull E, Ferrero M, Parcollet O, Georges A, Millis AJ (2010) Momentum-space anisotropy and pseudogaps: A comparative cluster dynamical mean-field analysis of the doping-driven metal-insulator transition in the two-dimensional Hubbard model. *Phys Rev B* 82(15):155101.
27. Shastry B (2011) Extremely correlated Fermi liquids. *Phys Rev Lett* 107(5):056404.
28. Bergeron D, Hankevych V, Kyung B, Tremblay AM (2011) Optical and dc conductivity of the two-dimensional Hubbard model in the pseudogap regime and across the antiferromagnetic quantum critical point including vertex corrections. *Phys Rev B* 84(8):085128.
29. Anderson PW (2008) Hidden Fermi liquid: The secret of high-T_c cuprates. *Phys Rev B* 78(17):174505.
30. Ioffe L, Millis A (1998) Zone-diagonal-dominated transport in high-T_c cuprates. *Phys Rev B* 58(17):11631–11637.
31. Stojkovic BP, Pines D (1997) Theory of the longitudinal and Hall conductivities of the cuprate superconductors. *Phys Rev B* 55(13):8576–8595.
32. Basov DN, Averitt RD, van der Marel D, Dressel M, Haule K (2011) Electrodynamics of correlated electron materials. *Rev Mod Phys* 83(2):471.
33. Dressel M (2011) Quantum criticality in organic conductors? Fermi liquid versus non-Fermi-liquid behaviour. *J Phys Condens Matter* 23(29):293201.
34. Nagel U, et al. (2012) Optical spectroscopy shows that the normal state of URu_2Si_2 is an anomalous Fermi liquid. *Proc Natl Acad Sci USA* 109(47):19161–19165.
35. Maslov D, Chubukov A (2012) First-Matsubara-frequency rule in a Fermi liquid. Part II: Optical conductivity and comparison to experiment. *Phys Rev B* 86(15):155137.
36. Chubukov A, Maslov D (2004) Singular corrections to the Fermi-liquid theory. *Phys Rev B* 69(12):121102.
37. Zhao X, et al. (2006) Crystal growth and characterization of the model high-temperature superconductor $HgBa_2CuO_{4+\delta}$. *Adv Mater (Deerfield Beach Fla)* 18 (24):3243–3247.
38. Barišić N, et al. (2008) Demonstrating the model nature of the high-temperature superconductor $HgBa_2CuO_{4+\delta}$. *Phys Rev B* 78(5):054518.

Supporting Information

Mirzaei et al. 10.1073/pnas.1218846110

I. Optical Spectroscopy

The infrared reflectivity of the *a*–*b* plane was measured at near-normal incidence using a Fourier-transform spectrometer (8 meV–1.24 eV). In addition, ellipsometric measurements were performed in the near-IR to near-UV using a Woolam variable angle spectroscopic ellipsometer (0.8–3.7 eV). The procedure of ref. 1 was used to suppress possible spurious *c*-axis components in the reflectance curves. The absolute value of the reflectivity was obtained by an in situ gold evaporation on the sample. The sample was mounted in a high-vacuum home-made cryostat designed for high stability during the thermal cycles, a prerequisite for absolute temperature dependence of the reflectivity. The operating pressure was 10^{-7} mbar. Temperature cool-down sweeps have been performed between 395 and 10 K at a speed of 0.9 K/min, leading to about one reflectivity spectrum per kelvin. To increase the signal-to-noise ratio, the data have been binned in 10-K temperature intervals. The long time-scale drift of the mid-IR detectors has been calibrated using a flipping mirror placed outside the cryostat in front of the sample. The absolute reflectivity calibrated for spectrometer throughput and drift is obtained from the relation

$$R(\omega)=\frac{I_{\text{sample}}(\omega)}{I_{\text{reference}}(\omega)}\frac{I_{\text{reference-mirror}}(\omega)}{I_{\text{sample-mirror}}(\omega)}. \qquad [S1]$$

The reflectivity spectra for selected temperatures are displayed in Fig. S1. As discussed in the main text, the consistency of this procedure is confirmed by the good correlation with the resistivity measurement shown. In addition, the *c*-axis reflectivity was measured at room temperature on a polished edge of the sample using an IR microscope attached to a conventional Fourier transform spectrometer. The frequency range of that measurement goes from 68 meV to 1.5 eV.

For frequencies above 0.8 eV we used spectroscopic ellipsometry with an angle of incidence set at 61° relative to the surface normal, providing after inversion of the Fresnel equations the so-called pseudodielectric function

$$\varepsilon_{ps}(\omega)=\sin^2\theta + \sin^4\theta\left(\frac{\sqrt{\varepsilon_{ab}-\sin^2\theta}\sqrt{\varepsilon_{ab}}-\sqrt{1-\varepsilon_c^{-1}\sin^2\theta}}{\sqrt{\varepsilon_{ab}-\sin^2\theta}\sqrt{1-\varepsilon_c^{-1}\sin^2\theta}-\sqrt{\varepsilon_{ab}}\cos^2\theta}\right)^2, \qquad [S2]$$

where ε_{ab} and ε_c are the dielectric tensor elements in the *a*–*b* plane and along the *c* axis, respectively. The dashed curves in Fig. S2 represent the pseudodielectric function measured at 300 K. In the limit of zero anisotropy ($\varepsilon_{ab}=\varepsilon_c$) the pseudodielectric function becomes the dielectric function ($\varepsilon_{ps}=\varepsilon_{ab}$). We corrected for the *c*-axis dielectric function by fitting the pseudodielectric function, the *a*–*b*-plane reflectance and the *c*-axis reflectivities to a Drude–Lorentz model. The resulting *a*–*b*-plane dielectric functions are shown in Fig. S2 for a few selected temperatures. The reflectance and phase spectra were calculated in this data range using the Fresnel expression for normal incidence reflectivity. A perfect match was obtained in the range of overlap (0.8–1.2 eV) of ellipsometry and direct normal incidence reflectance data. The complex dielectric constant was obtained by standard Kramers–Kronig transformation of the reflectance data, using the reflectance and phase data between 0.8 and 3.7 eV to fix the high-frequency extrapolation. This procedure anchors the phase output of the Kramers–Kronig transformation in the entire frequency range to the experimental data between 0.8 and 3.7 eV.

II. Drude–Lorentz Analysis

To characterize the oscillator strengths and frequencies corresponding to the interband transitions, we have fitted to the experimental conductivities a linear superposition of Drude and Lorentz oscillators

$$\varepsilon(\omega)=1+S_h+\sum_{j=0}^{N}\frac{\omega_{pj}^2}{\omega_j^2-\omega(\omega+i\gamma_j)}, \qquad [S3]$$

where S_h summarizes the dielectric polarizability originating in oscillators at frequencies higher than the $j=7$ mode at 5.2 eV. The dielectric function is understood to represent the superposition of the conduction electron (or hole) optical conductivity and the "bound charge" response

$$\varepsilon(\omega)=\frac{4\pi i}{\omega}\sigma_f(\omega)+\varepsilon_b(\omega). \qquad [S4]$$

The optical conductivity is shown in Fig. S3, together with the Drude–Lorentz fit. The corresponding parameters are summarized in Table S1.

III. Conduction Band and Bound Charge Contributions

Here we will interpret all oscillators below 1.2 eV as an intrinsic part of the conduction band response. The interpretation of the weak green peak at 1.4 eV is uncertain. Because the spectral weight is very small, it makes little difference for the discussion in the present paper whether or not we assume it to be part of the conduction band response. A reasonable approximation for the total (coherent + incoherent) conduction band spectral weight is therefore

$$\omega_p^2=\sum_{\hbar\omega_j<1.2\text{ eV}}\omega_{pj}^2. \qquad [S5]$$

The resulting value for $\hbar\omega_p$ is indicated in Table S1. An alternative scheme for determining the conduction band spectral weight consists of fitting the dielectric function in the full frequency range to a sum of bound charge oscillators above 1.2 eV and to use Allen's formula for the conduction band conductivity of electrons coupled to bosons (2–4), where in the latter the amplitudes of the blocks of a histogram representation of the electron–boson coupling function are adjusted to obtain the best fit.

The rise in optical conductivity above 1.8 eV is due to the onset of $O2p\rightarrow Cu3d$ charge-transfer transitions. The dielectric response described by the oscillators above 1.2 eV is therefore interpreted as bound charge response. The bound charge component of the dielectric function is

$$\varepsilon_b(\omega)=1+S_h+\sum_{\hbar\omega_j>1.2\text{ eV}}\frac{\omega_{pj}^2}{\omega_j^2-\omega(\omega+i\gamma_j)} \cong 1+S_h+\sum_{\hbar\omega_j>1.2\text{ eV}}\frac{\omega_{pj}^2}{\omega_j^2}. \qquad [S6]$$

The right-hand side of the expression is a valid approximation for the present set of data. This is demonstrated in Fig. S4,

showing Re $\varepsilon_b(\omega)$ and Im $\varepsilon_b(\omega)$ using the parameters in Table S1, together with the total dielectric function. We see that $\varepsilon_b(\omega) = 4.3 \pm 0.1$ everywhere in the frequency range shown.

IV. Sheet Conductance and Spectral Weight

We consider a cuprate with N_L conducting CuO_2 sheets per unit cell, having c-axis lattice parameter d_c. This corresponds to an average spacing $d_c = c/N_L$ between the CuO_2 sheets. The relation between sheet conductance and bulk conductivity is

$$G(\omega) = d_c \sigma(\omega). \qquad \textbf{[S7]}$$

The general expression for spectral weight of the sheet conductance along the x_j axis is (4)

$$K = \frac{d_c}{V} \sum_{k,\sigma} n_{k,\sigma} \frac{\partial^2 \varepsilon_{k,\sigma}}{\partial k_j^2}, \qquad \textbf{[S8]}$$

where $n_{k\sigma}$ is the average occupation of the state with momentum k and spin σ; V is the sample volume. For a parabolic dispersion relation ($\varepsilon_k = \hbar^2 k^2/2m$) the Fermi energy is πK. Ab initio local density approximation (LDA) band calculations for the cuprates can be accurately represented by the tight-binding expression

$$\begin{aligned} \varepsilon_k = & -2t\left[\cos(k_x a) + \cos(k_y a)\right] \\ & + 4t' \cos(k_x a)\cos(k_y a) - 2t'' \cos(2k_x a)\cos(2k_y a). \end{aligned} \qquad \textbf{[S9]}$$

We calculated K numerically as a function of hole density, inserting Eq. **S9** into Eq. **S8**, and adopting the parameter set appropriate to the case of Hg1201 (5): $t = 0.45$ eV, $t'/t = 0.35$, $t''/t' = 0.5$. The parametric plot of K versus hole density is presented in Fig. 3 of the main text (black solid curve).

V. Generalized Drude Analysis

The real part of the optical conductivity is shown in Fig. 1 of the main text for different temperatures. There is a clear signature of a pseudogap above T_c, with a maximum at ~0.15 eV. The phase of conduction band optical conductivity, shown in Fig. S5, has a gradual rise of phase as a function of frequency, in agreement with the behavior of underdoped Bi2212 pointed out in ref. 6, and distinctly different from $\sigma(\omega) = C(i\omega)^{-2/3}$ observed in optimally doped cuprates.

A generally used expression for the optical conductivity of a liquid of interacting electrons is the so-called extended Drude formula, expressed in the context of this article as a sheet conductance in units of $G_0 = 2e^2/h$:

$$G(\omega) = \frac{i\pi K}{\hbar\omega + M(\omega)} G_0, \qquad \textbf{[S10]}$$

where $M(\omega, T)$ is defined as a "memory function" (7) encoding the departure from standard Drude behavior caused, for instance, by electron–electron interactions or electron–phonon coupling. For a Fermi liquid, the imaginary part of $M(\omega, T)$ has a simple interpretation as the relaxation rate of the unrenormalized electrons, Im $M(\omega, T) = \hbar/\tau(\omega, T)$, and Re $M(\omega, T)/\hbar\omega + 1 = m^*(\omega, T)/m$ is the frequency-dependent mass renormalization.

The spectral weight factor K is related to the plasma frequency through the relation

$$\hbar^2 \omega_p^2 = \frac{4\pi e^2}{d_c} K. \qquad \textbf{[S11]}$$

With $\hbar\omega_p = 2.053$ eV (Table S1) and the c-axis parameter $d_c = 0.952$ nm we obtain $K = 222$ meV. The memory functions in Fig. 4 of the main text have been calculated from the optical conductivity using Eq. **S10**. The sharp features at 30, 40, 55, 70, 80, and 90 meV of the Hg1201 data are due to dipole active optical phonons. Although in principle these could be subtracted from the optical conductivity before calculating $M(\omega, T)$, this kind of subtraction procedure contains some ambiguities due to Fano-like phonon asymmetries. Because after subtraction these ambiguities are imported into the resulting memory function, we have refrained from subtracting the phonons. Instead, to facilitate comparison of different temperatures, in Figs. 5 and 6 of the main text narrow bands corresponding to the prominent sharp features at 80 and 90 meV of the UD Hg1201 data have been left open, as can be seen in Fig. 5 of the main text.

VI. Memory Function of a Local Fermi Liquid

For a system whose carriers can be well described by a local (i.e., momentum-independent) scattering rate, the optical conductivity can be expressed entirely in terms of the complex electronic self-energy $\Sigma(\varepsilon) \equiv \Sigma_1(\varepsilon) + i\Sigma_2(\varepsilon)$. The scattering rate is $-\Sigma_2$, and Σ_1 is linked to Σ_2 by a Kramers–Kronig transformation. This happens because, for a local self-energy, the vertex corrections vanish in the Kubo formula for the conductivity $\sigma(\omega)$. As a result,

$$\sigma(\omega, T) = \int d\varepsilon \frac{i\Phi(0)}{\omega} \frac{f(\varepsilon) - f(\varepsilon + \hbar\omega)}{\hbar\omega + \Sigma^*(\varepsilon) - \Sigma(\varepsilon + \hbar\omega)}. \qquad \textbf{[S12]}$$

Here, $f(\varepsilon) = [\exp(\varepsilon/k_B T) + 1]^{-1}$, and $\Phi(0)$ is proportional to the Fermi surface average of the square of the bare electronic group velocity. In a Fermi liquid, the quasi-particles are well-defined at low temperature close to the Fermi surface, because in this limit the scattering rate vanishes with a characteristic energy and temperature dependence proportional to $\varepsilon^2 + (\pi k_B T)^2$. The quasi-particle spectral weight Z is smaller than unity, as reflected by the fact that $\Sigma_1(\varepsilon)$ has a finite negative slope $1 - 1/Z$ at $\varepsilon = 0$. This leads to the following low-energy model for the self-energy of a local Fermi liquid:

$$\Sigma(\varepsilon) = \left(1 - \frac{1}{Z}\right)\varepsilon - \frac{3}{2} iC\left[\varepsilon^2 + \pi^2 (k_B T)^2\right]. \qquad \textbf{[S13]}$$

The added factor 3/2 anticipates the formula for the memory function. In systems where all properties are set by a single characteristic energy D, as in isotropic doped Mott insulators where D is typically the half bandwidth, the coefficient C would be proportional to $1/(Z^2 D)$. Indeed, in such cases the scattering rate $-\Sigma_2(0)$ scales with renormalized electronic energies as $D(k_B T/ZD)^2$. The quasi-particle lifetime controls the Drude response at very low frequencies. On the Fermi surface, it can be computed from the self-energy as $\tau_{qp} = \hbar/(2Z|\Sigma_2(0)|)$. We are interested in the regime of frequencies much larger than $1/\tau_{qp}$: introducing Eq. **S13** into Eq. **S12**, and expanding for large $\omega\tau_{qp}$, we get (8)

$$\begin{aligned} \sigma(\omega, T) = & \Phi(0) Z \tau_{qp} \left\{ \frac{i}{\omega\tau_{qp}} + \frac{4}{3(\omega\tau_{qp})^2} \left[1 + \left(\frac{\hbar\omega}{2\pi k_B T}\right)^2\right] \right\} \\ & + O\left[1/(\omega\tau_{qp})^3\right]. \end{aligned} \qquad \textbf{[S14]}$$

Comparing this with Eq. **1** of the main text, we obtain Eq. **2** of the main text in the regime $\omega\tau_{qp} \gg 1$, where $\tilde{Z} \sim Z\Phi(0)/K$.

VII. Scaling Collapse

We tested the frequency and temperature dependence of the imaginary part of the memory function for scaling collapse of the form of Eq. **2** of the main text by plotting of the data in the normal state as a function of $\xi^2 = (\hbar\omega)^2 + (p\pi k_B T)^2$, and searching for the value of p that provides the best overlap of the low-ξ data for the spectra taken at different temperatures. As we see in Fig. S6,

neither for $p=1$ nor for $p=2$ do the data collapse on a single curve. The optimal value where the data does collapse, $p=1.5$, is used in Fig. 5 of the main text. Note that the data above 320 K correspond to the plateau at high frequencies, which is clearly outside the range of validity of single-parameter scaling. For this reason the data shown in Fig. 5 of the main text were restricted to the temperatures below 320 K. In ref. 6 a different scaling relation—pertaining to the real part of the optical conductivity—was reported:

$$\frac{\hbar}{k_B T \sigma_1(\omega,T)} = \frac{4\pi}{\omega_p^2}\left(1+A^2\left(\frac{\hbar\omega}{k_B T}\right)^2\right), \qquad \textbf{[S15]}$$

where A is a number of order 1. This is the classical relaxation dynamics expected near a quantum critical point (9). One may wonder whether this behavior can occur together with single-parameter scaling of the form $M_2(\omega,T)=M_2(\xi)$, i.e., similar to Eq. **2** of the main text but not necessarily corresponding to a ξ^2-dependence of M_2. The aforementioned scaling relation of $T\sigma_1(\omega,T)$ can be obtained if $M_2(\omega,T)=iA^{-1}k_B T$ for $\omega/T\to 0$. Because in this limit $\xi=k_B T$, consequently M_2 has a linear dependence on ξ, at least for not too large ξ. However, lacking a theoretical justification for scaling of the form $M_2(\omega,T)=M_2(\xi)$ for systems which are not a Fermi liquid, we restrict the present discussion to the underdoped cuprates in the pseudogap phase.

1. van Heumen E, et al. (2007) Optical and thermodynamic properties of the high-temperature superconductor $HgBa_2CuO_{4+\delta}$. *Phys Rev B* 75(5):054522.
2. van Heumen E, Meevasana W, Kuzmenko AB, Eisaki H, van der Marel D (2009) Doping-dependent optical properties of Bi2201. *New J Phys* 11(5):055067.
3. Allen PB (1971) Electron-phonon effects in the infrared properties of metals. *Phys Rev B* 3(2):305–320.
4. Norman M, Chubukov A, van Heumen E, Kuzmenko AB, van der Marel D (2007) Optical integral in the cuprates and the question of sum-rule violation. *Phys Rev B* 76(22): 220509.
5. Pavarini E, Dasgupta I, Saha-Dasgupta T, Jepsen O, Andersen OK (2001) Band-structure trend in hole-doped cuprates and correlation with T(c max). *Phys Rev Lett* 87(4):047003.
6. van der Marel D, et al. (2003) Quantum critical behaviour in a high-T(c) superconductor. *Nature* 425(6955):271–274.
7. Götze W, Wölfle P (1972) Homogeneous dynamical conductivity of simple metals. *Phys Rev B* 6(4):1226–1238.
8. Berthod C, et al. (2013) Non-Drude universal scaling laws for the optical response of local Fermi liquids *Phys Rev B* 87(11):115109.
9. Sachdev S (1999) *Quantum Phase Transitions* (Cambridge Univ Press, Cambridge, UK).

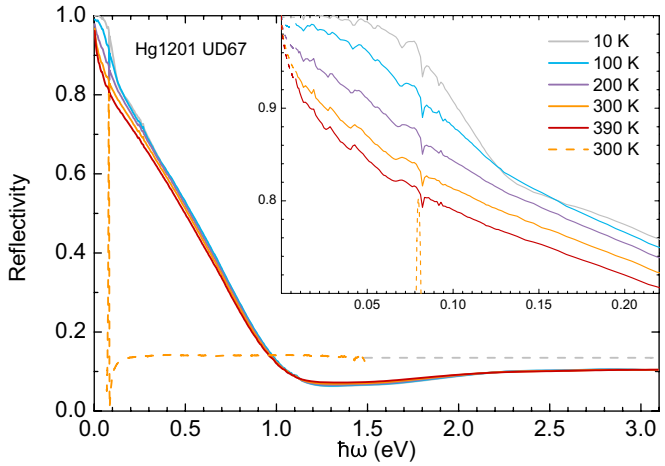

Fig. S1. Optical reflectivity of $HgBa_2CuO_{4+\delta}$ UD67 along the *a*- (solid lines) and *c* (dashed line) axes at selected temperatures. A strong phonon mode is observed in both *a* and *c* axes at 82 meV. (*Inset*) Far infrared reflectivity; it is also possible to see the remainder of a suppressed *c*-axis phonon at 70 meV.

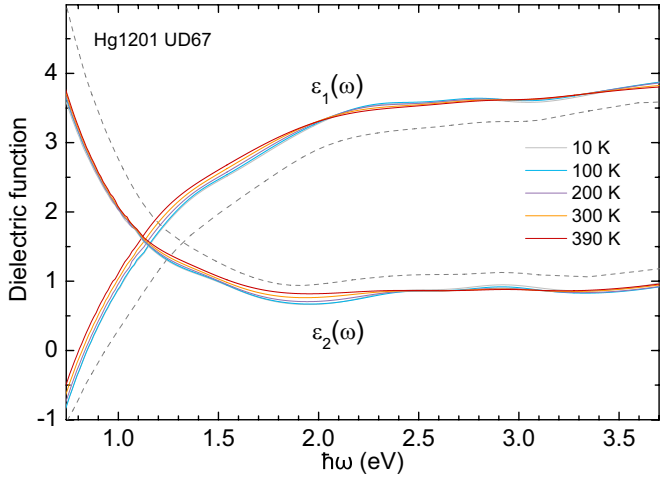

Fig. S2. Real and imaginary parts of the pseudodielectric function (dashed curves) obtained from ellipsometry at room temperature, and *a*–*b*-plane dielectric function at selected temperatures corrected using the method explained in the text.

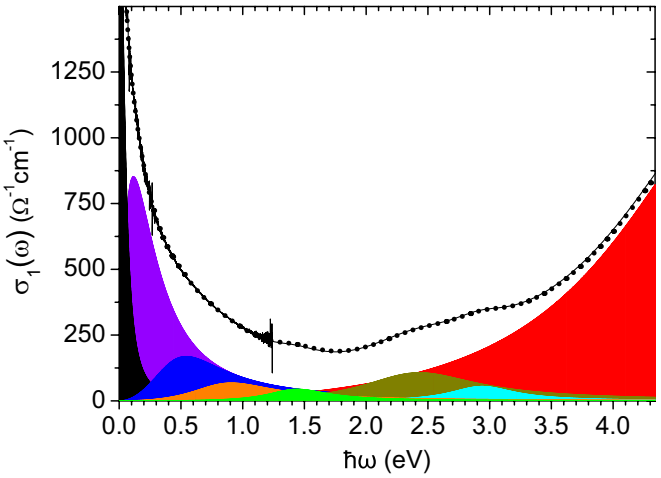

Fig. S3. Drude–Lorentz fit to the real part of the optical conductivity, $\sigma_1(\omega)$, at 300 K. The four Lorentzians above 1.2 eV are interpreted as bound charge contributions to $\sigma_1(\omega)$. The dotted gray curve is the sum of all oscillators which matches perfectly the $\sigma_1(\omega)$ calculated from Kramers–Kronig transformation (thin black curve).

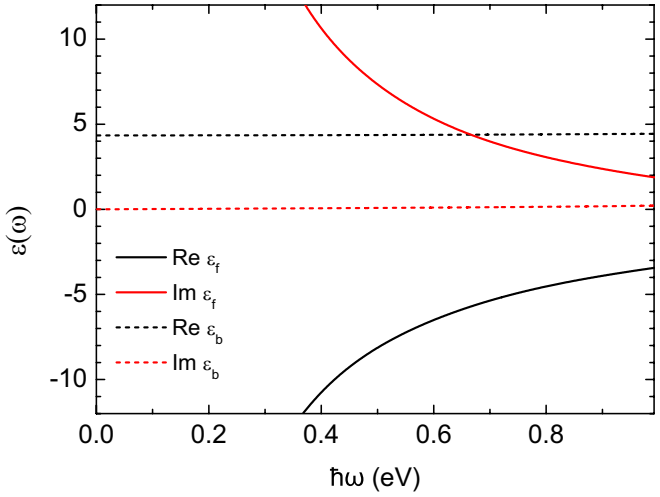

Fig. S4. Total (solid curves) and bound charge dielectric function (last four oscillators of Table S1) at room temperature. To a very good approximation $\varepsilon_b = 4.3 \pm 0.1$ with negligible imaginary part in the entire frequency range shown.

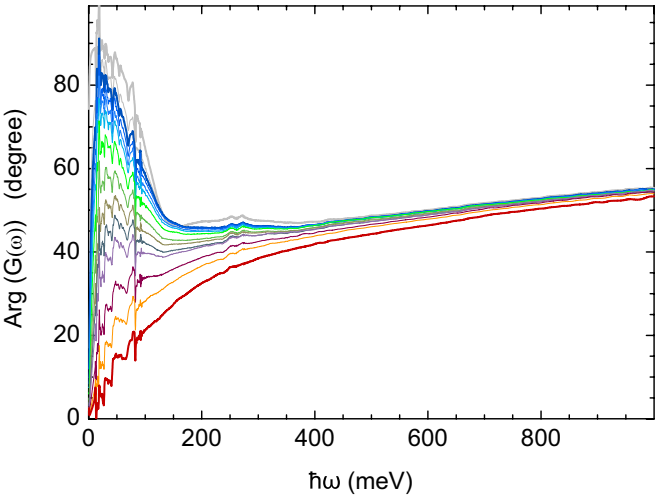

Fig. S5. Phase of the optical sheet conductance for UD Hg1201. Temperatures from 10 to 390 K. Data below T_c are shown in gray.

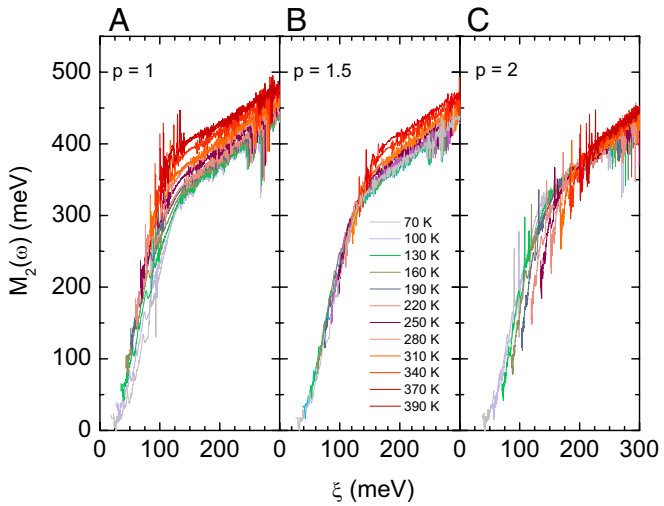

Fig. S6. Imaginary part of the memory function as a function of ξ, where $\xi^2 = (\hbar\omega)^2 + (p\pi k_B T)^2$ with (*A*) $p = 1$, (*B*) $p = 1.5$, and (*C*) $p = 2$ for underdoped Hg1201 ($T_c = 67$ K). The data correspond to the normal state.

Table S1. Parameters of the Drude–Lorentz oscillators displayed in Fig. S3

Parameters	$j = 0$	$j = 1$	$j = 2$	$j = 3$	$\hbar\omega_p$	$j = 4$	$j = 5$	$j = 6$	$j = 7$	S_h
$\hbar\omega_{0,j}$	0	0.116	0.542	0.908	—	1.443	2.430	2.939	5.204	—
$\hbar\omega_{p,j}$	0.857	1.461	0.969	0.638	2.053	0.444	0.947	0.510	4.390	2.2
$\hbar\gamma_{0,j}$	0.046	0.337	0.747	0.805	—	0.598	1.126	0.636	2.723	—

S_h is dimensionless. Parameter values corresponding to $\hbar\omega_p$, $\hbar\omega_0$, and $\hbar\gamma$ are in units of electronvolts.